Search for a light sterile neutrino with 7.5 years of IceCube DeepCore data

R. Abbasi,[17] M. Ackermann,[65] J. Adams,[18] S. K. Agarwalla,[40,*] J. A. Aguilar,[12] M. Ahlers,[22] J. M. Alameddine,[23] N. M. Amin,[44] K. Andeen,[42] C. Argüelles,[14] Y. Ashida,[53] S. Athanasiadou,[65] L. Ausborm,[1] S. N. Axani,[44] X. Bai,[50] A. Balagopal V.,[40] M. Baricevic,[40] S. W. Barwick,[30] S. Bash,[27] V. Basu,[40] R. Bay,[8] J. J. Beatty,[20,21] J. Becker Tjus,[11,†] J. Beise,[63] C. Bellenghi,[27] C. Benning,[1] S. BenZvi,[52] D. Berley,[19] E. Bernardini,[48] D. Z. Besson,[36] E. Blaufuss,[19] L. Bloom,[60] S. Blot,[65] F. Bontempo,[31] J. Y. Book Motzkin,[14] C. Boscolo Meneguolo,[48] S. Böser,[41] O. Botner,[63] J. Böttcher,[1] E. Bourbeau,[22] J. Braun,[40] B. Brinson,[6] J. Brostean-Kaiser,[65] L. Brusa,[1] R. T. Burley,[2] D. Butterfield,[40] M. A. Campana,[49] I. Caracas,[41] K. Carloni,[14] J. Carpio,[34,35] S. Chattopadhyay,[40,‡] N. Chau,[12] Z. Chen,[56] D. Chirkin,[40] S. Choi,[57,58] B. A. Clark,[19] A. Coleman,[63] G. H. Collin,[15] A. Connolly,[20,21] J. M. Conrad,[15] R. Corley,[53] D. F. Cowen,[61,62] P. Dave,[6] C. De Clercq,[13] J. J. DeLaunay,[60] D. Delgado,[14] S. Deng,[1] A. Desai,[40] P. Desiati,[40] K. D. de Vries,[13] G. de Wasseige,[37] T. DeYoung,[24] A. Diaz,[15] J. C. Díaz-Vélez,[40] P. Dierichs,[1] M. Dittmer,[43] A. Domi,[26] L. Draper,[53] H. Dujmovic,[40] D. Durnford,[25] K. Dutta,[41] M. A. DuVernois,[40] T. Ehrhardt,[41] L. Eidenschink,[27] A. Eimer,[26] P. Eller,[27] E. Ellinger,[64] S. El Mentawi,[1] D. Elsässer,[23] R. Engel,[31,32] H. Erpenbeck,[40] J. Evans,[19] P. A. Evenson,[44] K. L. Fan,[19] K. Fang,[40] K. Farrag,[16] A. R. Fazely,[7] A. Fedynitch,[59] N. Feigl,[10] S. Fiedlschuster,[26] C. Finley,[55] L. Fischer,[65] D. Fox,[61] A. Franckowiak,[11] S. Fukami,[65] P. Fürst,[1] J. Gallagher,[39] E. Ganster,[1] A. Garcia,[14] M. Garcia,[44] G. Garg,[40,‡] E. Genton,[14,37] L. Gerhardt,[9] A. Ghadimi,[60] C. Girard-Carillo,[41] C. Glaser,[63] T. Glüsenkamp,[26,63] J. G. Gonzalez,[44] S. Goswami,[34,35] A. Granados,[24] D. Grant,[24] S. J. Gray,[19] O. Gries,[1] S. Griffin,[40] S. Griswold,[52] K. M. Groth,[22] D. Guevel,[40] C. Günther,[1] P. Gutjahr,[23] C. Ha,[54] C. Haack,[26] A. Hallgren,[63] L. Halve,[1] F. Halzen,[40] H. Hamdaoui,[56] M. Ha Minh,[27] M. Handt,[1] K. Hanson,[40] J. Hardin,[15] A. A. Harnisch,[24] P. Hatch,[33] A. Haungs,[31] J. Häußler,[1] K. Helbing,[64] J. Hellrung,[11] J. Hermannsgabner,[1] L. Heuermann,[1] N. Heyer,[63] S. Hickford,[64] A. Hidvegi,[55] J. Hignight,[66] C. Hill,[16] G. C. Hill,[2] K. D. Hoffman,[19] S. Hori,[40] K. Hoshina,[40,§] M. Hostert,[14] W. Hou,[31] T. Huber,[31] K. Hultqvist,[55] M. Hünnefeld,[23] R. Hussain,[40] K. Hymon,[23,59] A. Ishihara,[16] W. Iwakiri,[16] M. Jacquart,[40] S. Jain,[41] O. Janik,[26] M. Jansson,[55] G. S. Japaridze,[5] M. Jeong,[53] M. Jin,[14] B. J. P. Jones,[4] N. Kamp,[14] D. Kang,[31] W. Kang,[57] X. Kang,[49] A. Kappes,[43] D. Kappesser,[41] L. Kardum,[23] T. Karg,[65] M. Karl,[27] A. Karle,[40] A. Katil,[25] U. Katz,[26] M. Kauer,[40] J. L. Kelley,[40] M. Khanal,[53] A. Khatee Zathul,[40] A. Kheirandish,[34,35] J. Kiryluk,[56] S. R. Klein,[8,9] A. Kochocki,[24] R. Koirala,[44] H. Kolanoski,[10] T. Kontrimas,[27] L. Köpke,[41] C. Kopper,[26] D. J. Koskinen,[22] P. Koundal,[44] M. Kovacevich,[49] M. Kowalski,[10,65] T. Kozynets,[22] J. Krishnamoorthi,[40,‡] K. Kruiswijk,[37] E. Krupczak,[24] A. Kumar,[65] E. Kun,[11] N. Kurahashi,[49] N. Lad,[65] C. Lagunas Gualda,[65] M. Lamoureux,[37] M. J. Larson,[19] S. Latseva,[1] F. Lauber,[64] J. P. Lazar,[37] J. W. Lee,[57] K. Leonard DeHolton,[62] A. Leszczyńska,[44] J. Liao,[6] M. Lincetto,[11] Y. T. Liu,[62] M. Liubarska,[25] C. Love,[49] L. Lu,[40] F. Lucarelli,[28] W. Luszczak,[20,21] Y. Lyu,[8,9] W. Y. Ma,[67] J. Madsen,[40] E. Magnus,[13] K. B. M. Mahn,[24] Y. Makino,[40] E. Manao,[27] S. Mancina,[40,48] W. Marie Sainte,[40] I. C. Mariş,[12] S. Marka,[46] Z. Marka,[46] M. Marsee,[60] I. Martinez-Soler,[14] R. Maruyama,[45] F. Mayhew,[24] F. McNally,[38] J. V. Mead,[22] K. Meagher,[40] S. Mechbal,[65] A. Medina,[21] M. Meier,[16] Y. Merckx,[13] L. Merten,[11] J. Micallef,[24] J. Mitchell,[7] T. Montaruli,[28] R. W. Moore,[25] Y. Morii,[16] R. Morse,[40] M. Moulai,[40] T. Mukherjee,[31] R. Naab,[65] R. Nagai,[16] M. Nakos,[40] U. Naumann,[64] J. Necker,[65] A. Negi,[4] L. Neste,[55] M. Neumann,[43] H. Niederhausen,[24] M. U. Nisa,[24] K. Noda,[16] A. Noell,[1] A. Novikov,[44] A. Obertacke Pollmann,[16] V. O'Dell,[40] B. Oeyen,[29] A. Olivas,[19] R. Orsoe,[27] J. Osborn,[40] E. O'Sullivan,[63] V. Palusova,[41] H. Pandya,[44] N. Park,[33] G. K. Parker,[4] E. N. Paudel,[44] L. Paul,[50] C. Pérez de los Heros,[63] T. Pernice,[65] J. Peterson,[40] A. Pizzuto,[40] M. Plum,[50] A. Pontén,[63] Y. Popovych,[41] M. Prado Rodriguez,[40] B. Pries,[24] R. Procter-Murphy,[19] G. T. Przybylski,[9] C. Raab,[37] J. Rack-Helleis,[41] M. Ravn,[63] K. Rawlins,[3] Z. Rechav,[40] A. Rehman,[44] P. Reichherzer,[11] E. Resconi,[27] S. Reusch,[65] W. Rhode,[23] B. Riedel,[40] A. Rifaie,[1] E. J. Roberts,[2] S. Robertson,[8,9] S. Rodan,[57,58] G. Roellinghoff,[57] M. Rongen,[26] A. Rosted,[16] C. Rott,[53,57] T. Ruhe,[23] L. Ruohan,[27] D. Ryckbosch,[29] I. Safa,[40] J. Saffer,[32] D. Salazar-Gallegos,[24] P. Sampathkumar,[31] A. Sandrock,[64] M. Santander,[60] S. Sarkar,[25] S. Sarkar,[47] J. Savelberg,[1] P. Savina,[40] P. Schaile,[27] M. Schaufel,[1] H. Schieler,[31] S. Schindler,[26] L. Schlickmann,[41] B. Schlüter,[43] F. Schlüter,[12] N. Schmeisser,[64] T. Schmidt,[19] J. Schneider,[26] F. G. Schröder,[31,44] L. Schumacher,[26] S. Sclafani,[19] D. Seckel,[44] M. Seikh,[36] M. Seo,[57] S. Seunarine,[51] P. Sevle Myhr,[37] R. Shah,[49] S. Shefali,[32] N. Shimizu,[16] M. Silva,[40] B. Skrzypek,[8] B. Smithers,[4] R. Snihur,[40] J. Soedingrekso,[23] A. Søgaard,[22] D. Soldin,[53] P. Soldin,[1] G. Sommani,[11] C. Spannfellner,[27] G. M. Spiczak,[51] C. Spiering,[65] M. Stamatikos,[21] T. Stanev,[44] T. Stezelberger,[9] T. Stürwald,[64] T. Stuttard,[22] G. W. Sullivan,[19] I. Taboada,[6] S. Ter-Antonyan,[7] A. Terliuk,[27] M. Thiesmeyer,[1] W. G. Thompson,[14] J. Thwaites,[40] S. Tilav,[44] K. Tollefson,[24] C. Tönnis,[57] S. Toscano,[12] D. Tosi,[40] A. Trettin,[65] R. Turcotte,[31] J. P. Twagirayezu,[24] M. A. Unland Elorrieta,[43] A. K. Upadhyay,[40,*] K. Upshaw,[7] A. Vaidyanathan,[42] N. Valtonen-Mattila,[63] J. Vandenbroucke,[40] N. van Eijndhoven,[13] D. Vannerom,[15] J. van Santen,[65] J. Vara,[43] F. Varsi,[32] J. Veitch-Michaelis,[40] M. Venugopal,[31] M. Vereecken,[37] S. Vergara Carrasco,[18] S. Verpoest,[44] D. Veske,[46] A. Vijai,[19] C. Walck,[55] A. Wang,[6] C. Weaver,[24] P. Weigel,[15] A. Weindl,[31] J. Weldert,[62] A. Y. Wen,[14] C. Wendt,[40] J. Werthebach,[23]

M. Weyrauch,[31] N. Whitehorn,[24] C. H. Wiebusch,[1] D. R. Williams,[60] L. Witthaus,[23] A. Wolf,[1] M. Wolf,[27] G. Wrede,[26] X. W. Xu,[7] J. P. Yanez,[25] E. Yildizci,[40] S. Yoshida,[16] R. Young,[36] S. Yu,[53] T. Yuan,[40] Z. Zhang,[56] P. Zhelnin,[14] P. Zilberman,[40] and M. Zimmerman[40]

(IceCube Collaboration)

[1]*III. Physikalisches Institut, RWTH Aachen University, D-52056 Aachen, Germany*
[2]*Department of Physics, University of Adelaide, Adelaide, 5005, Australia*
[3]*Department of Physics and Astronomy, University of Alaska Anchorage, 3211 Providence Drive, Anchorage, Alaska 99508, USA*
[4]*Department of Physics, University of Texas at Arlington, 502 Yates Street, Science Hall Rm 108, Box 19059, Arlington, Texas 76019, USA*
[5]*CTSPS, Clark-Atlanta University, Atlanta, Geogia 30314, USA*
[6]*School of Physics and Center for Relativistic Astrophysics, Georgia Institute of Technology, Atlanta, Georgia 30332, USA*
[7]*Department of Physics, Southern University, Baton Rouge, Louisiana 70813, USA*
[8]*Department of Physics, University of California, Berkeley, California 94720, USA*
[9]*Lawrence Berkeley National Laboratory, Berkeley, California 94720, USA*
[10]*Institut für Physik, Humboldt-Universität zu Berlin, D-12489 Berlin, Germany*
[11]*Fakultät für Physik & Astronomie, Ruhr-Universität Bochum, D-44780 Bochum, Germany*
[12]*Université Libre de Bruxelles, Science Faculty CP230, B-1050 Brussels, Belgium*
[13]*Vrije Universiteit Brussel (VUB), Dienst ELEM, B-1050 Brussels, Belgium*
[14]*Department of Physics and Laboratory for Particle Physics and Cosmology, Harvard University, Cambridge, Massachusetts 02138, USA*
[15]*Department of Physics, Massachusetts Institute of Technology, Cambridge, Massachusetts 02139, USA*
[16]*Department of Physics and The International Center for Hadron Astrophysics, Chiba University, Chiba 263-8522, Japan*
[17]*Department of Physics, Loyola University Chicago, Chicago, Illinois 60660, USA*
[18]*Department of Physics and Astronomy, University of Canterbury, Private Bag 4800, Christchurch, New Zealand*
[19]*Department of Physics, University of Maryland, College Park, Maryland 20742, USA*
[20]*Department of Astronomy, Ohio State University, Columbus, Ohio 43210, USA*
[21]*Department of Physics and Center for Cosmology and Astro-Particle Physics, Ohio State University, Columbus, Ohio 43210, USA*
[22]*Niels Bohr Institute, University of Copenhagen, DK-2100 Copenhagen, Denmark*
[23]*Department of Physics, TU Dortmund University, D-44221 Dortmund, Germany*
[24]*Department of Physics and Astronomy, Michigan State University, East Lansing, Michigan 48824, USA*
[25]*Department of Physics, University of Alberta, Edmonton, Alberta, T6G 2E1, Canada*
[26]*Erlangen Centre for Astroparticle Physics, Friedrich-Alexander-Universität Erlangen-Nürnberg, D-91058 Erlangen, Germany*
[27]*Physik-department, Technische Universität München, D-85748 Garching, Germany*
[28]*Département de physique nucléaire et corpusculaire, Université de Genève, CH-1211 Genève, Switzerland*
[29]*Department of Physics and Astronomy, University of Gent, B-9000 Gent, Belgium*
[30]*Department of Physics and Astronomy, University of California, Irvine, California 92697, USA*
[31]*Karlsruhe Institute of Technology, Institute for Astroparticle Physics, D-76021 Karlsruhe, Germany*
[32]*Karlsruhe Institute of Technology, Institute of Experimental Particle Physics, D-76021 Karlsruhe, Germany*
[33]*Department of Physics, Engineering Physics, and Astronomy, Queen's University, Kingston, Ontario K7L 3N6, Canada*
[34]*Department of Physics & Astronomy, University of Nevada, Las Vegas, Nevada 89154, USA*
[35]*Nevada Center for Astrophysics, University of Nevada, Las Vegas, Nevada 89154, USA*
[36]*Department of Physics and Astronomy, University of Kansas, Lawrence, Kansas 66045, USA*
[37]*Centre for Cosmology, Particle Physics and Phenomenology - CP3, Université catholique de Louvain, Louvain-la-Neuve, Belgium*
[38]*Department of Physics, Mercer University, Macon, Georgia 31207-0001, USA*
[39]*Department of Astronomy, University of Wisconsin—Madison, Madison, Wisconsin 53706, USA*
[40]*Department of Physics and Wisconsin IceCube Particle Astrophysics Center, University of Wisconsin—Madison, Madison, Wisconsin 53706, USA*

[41]Institute of Physics, University of Mainz, Staudinger Weg 7, D-55099 Mainz, Germany
[42]Department of Physics, Marquette University, Milwaukee, Wisconsin 53201, USA
[43]Institut für Kernphysik, Westfälische Wilhelms-Universität Münster, D-48149 Münster, Germany
[44]Bartol Research Institute and Department of Physics and Astronomy, University of Delaware, Newark, Delaware 19716, USA
[45]Department of Physics, Yale University, New Haven, Connecticut 06520, USA
[46]Columbia Astrophysics and Nevis Laboratories, Columbia University, New York, New York 10027, USA
[47]Department of Physics, University of Oxford, Parks Road, Oxford OX1 3PU, United Kingdom
[48]Dipartimento di Fisica e Astronomia Galileo Galilei, Università Degli Studi di Padova, I-35122 Padova PD, Italy
[49]Department of Physics, Drexel University, 3141 Chestnut Street, Philadelphia, Pennsylvania 19104, USA
[50]Physics Department, South Dakota School of Mines and Technology, Rapid City, South Dakota 57701, USA
[51]Department of Physics, University of Wisconsin, River Falls, Wisconsin 54022, USA
[52]Department of Physics and Astronomy, University of Rochester, Rochester, New York 14627, USA
[53]Department of Physics and Astronomy, University of Utah, Salt Lake City, Utah 84112, USA
[54]Department of Physics, Chung-Ang University, Seoul 06974, Republic of Korea
[55]Oskar Klein Centre and Department of Physics, Stockholm University, SE-10691 Stockholm, Sweden
[56]Department of Physics and Astronomy, Stony Brook University, Stony Brook, New York 11794-3800, USA
[57]Department of Physics, Sungkyunkwan University, Suwon 16419, Republic of Korea
[58]Institute of Basic Science, Sungkyunkwan University, Suwon 16419, Republic of Korea
[59]Institute of Physics, Academia Sinica, Taipei, 11529, Taiwan
[60]Department of Physics and Astronomy, University of Alabama, Tuscaloosa, Alabama 35487, USA
[61]Department of Astronomy and Astrophysics, Pennsylvania State University, University Park, Pennsylvania 16802, USA
[62]Department of Physics, Pennsylvania State University, University Park, Pennsylvania 16802, USA
[63]Department of Physics and Astronomy, Uppsala University, Box 516, SE-75120 Uppsala, Sweden
[64]Department of Physics, University of Wuppertal, D-42119 Wuppertal, Germany
[65]Deutsches Elektronen-Synchrotron DESY, Platanenallee 6, D-15738 Zeuthen, Germany
[66]Department of Physics, University of Alberta, Edmonton, Alberta, Canada T6G 2E1
[67]Deutsches Elektronen-Synchrotron DESY, Platanenallee 6, 15738 Zeuthen, Germany

(Received 2 July 2024; accepted 8 September 2024; published 15 October 2024)

We present a search for an eV-scale sterile neutrino using 7.5 years of data from the IceCube DeepCore detector. The analysis uses a sample of 21,914 events with energies between 5 and 150 GeV to search for sterile neutrinos through atmospheric muon neutrino disappearance. Improvements in event selection and treatment of systematic uncertainties provide greater statistical power compared to previous DeepCore sterile neutrino searches. Our results are compatible with the absence of mixing between active and sterile neutrino states, and we place constraints on the mixing matrix elements $|U_{\mu 4}|^2 < 0.0534$ and $|U_{\tau 4}|^2 < 0.0574$ at 90% CL under the assumption that $\Delta m^2_{41} \geq 1$ eV^2. These null results add to the growing tension between anomalous appearance results and constraints from disappearance searches in the $3+1$ sterile neutrino landscape.

DOI: 10.1103/PhysRevD.110.072007

[*]Also at Institute of Physics, Sachivalaya Marg, Sainik School Post, Bhubaneswar 751005, India.
[†]Also at Department of Space, Earth and Environment, Chalmers University of Technology, 412 96 Gothenburg, Sweden.
[‡]Also at Institute of Physics, Sachivalaya Marg, Sainik School Post, Bhubaneswar 751005, India.
[§]Also at Earthquake Research Institute, University of Tokyo, Bunkyo, Tokyo 113-0032, Japan.

I. INTRODUCTION

While the three-neutrino oscillation framework has been remarkably successful in explaining most observations of neutrino flavor transitions, several anomalies have emerged from various experiments that cannot be reconciled within this paradigm. Notably, the LSND and MiniBooNE experiments have reported an excess of electron-neutrinolike events in muon neutrino beams [1,2], which could be explained by the existence of a fourth, sterile neutrino species with a mass splitting of approximately 1 eV^2 relative to the three active neutrino flavors. This interpretation is further supported by the long-standing Gallium anomaly [3], a deficit of electron-neutrinos observed in radioactive source experiments that has been recently confirmed by the BEST and SAGE experiments [4,5]. These intriguing anomalies have motivated extensive efforts to search for sterile neutrinos in the eV mass range.

Although the sterile neutrinos do not directly interact via the weak force, they can mix with the active neutrino flavor eigenstates in a way that influences their oscillation behavior. The simplest mathematical description of the effect is the so-called $3+1$ model, in which a fourth mass eigenstate with mass splitting Δm^2_{41} and a noninteracting flavor eigenstate ν_s is added to the standard three-flavor model. The PMNS matrix [6] is extended by a fourth row and column, such that

$$U^{3+1}_{\mathrm{PMNS}} = \begin{pmatrix} U_{e1} & U_{e2} & U_{e3} & U_{e4} \\ U_{\mu 1} & U_{\mu 2} & U_{\mu 3} & U_{\mu 4} \\ U_{\tau 1} & U_{\tau 2} & U_{\tau 3} & U_{\tau 4} \\ U_{s1} & U_{s2} & U_{s3} & U_{s4} \end{pmatrix}. \tag{1}$$

The matrix elements $U_{\ell 4}$ determine the amount of mixing between the neutrino flavor ℓ and the fourth mass eigenstate. In this paradigm, the $\nu_\mu \to \nu_e$ flavor transition probability for short baseline experiments such as LSND and MiniBooNE is approximately proportional to the product $|U_{\mu 4}|^2|U_{e4}|^2$, while the ν_e survival probability measured in Gallium experiments depends only on the value of $|U_{e4}|^2$ [7].

The landscape of experimental tests of this model currently shows a highly conflicted picture. While the aforementioned anomalies are statistically highly significant, the mixing amplitudes $|U_{e4}|$ and $|U_{\mu 4}|$ that would be necessary to explain them are in strong tension with the combined nonanomalous measurements of the disappearance channels $\nu_\mu \to \nu_\mu$ and $\nu_e \to \nu_e$, which favor standard three-flavor neutrino mixing [7,8]. This includes previous measurements performed by IceCube DeepCore using atmospheric muon neutrinos, which to date have seen no significant sterile neutrino signal [9–11]. Measurements of the electron neutrino spectrum at the MicroBooNE experiment, a liquid argon time projection chamber targeted by the same neutrino beam as MiniBooNE, also failed to reproduce an anomalous low-energy excess [12,13]. Other measurements from accelerator neutrino sources that are compatible with the absense of sterile neutrino mixing were performed by NOνA [14] and MINOS/MINOS+ [15]. Several reactor neutrino experiments that use a near and far detector setup to cancel uncertainties of the initial neutrino flux also find no evidence for nonstandard neutrino oscillations [16–20]. Global constraints on the unitarity of the PMNS matrix derived from nonanomalous results furthermore limit the magnitudes of $|U_{e4}|^2$ and $|U_{\mu 4}|^2$ to $\mathcal{O}(10^{-3})$ and $\mathcal{O}(10^{-2})$, respectively [21]. The amplitude $|U_{\tau 4}|^2$ is currently only constrained to $\mathcal{O}(0.1)$. Furthermore, the number of relativistic neutrino species and the sum of neutrino masses can be constrained from cosmological observations. Sterile neutrinos could travel long distances unimpeded and therefore wash out the formation of structures at small scales in the early universe, which in turn would influence the power spectrum of the CMB and the formation of large structures. Recent constraints from the Planck Collaboration for these parameters are $N_{\mathrm{eff}} = 2.99(17)$ and $\sum m_\nu < 0.1$ eV, and strongly disfavor the existence of sterile neutrinos within the standard ΛCDM paradigm [22].

The tension between highly significant anomalies in some experiments and strong exclusions from others is one of the most pressing problems in the field of neutrino physics. Its resolution necessitates the combination of independent and complementary measurements from various experiments probing different oscillation channels and energy ranges that are affected by different systematic uncertainties. This work uses atmospheric muon neutrinos to constrain the mixing amplitudes $|U_{\mu 4}|^2$ and $|U_{\tau 4}|^2$ under the assumption that $\Delta m^2_{41} \geq 1$ eV^2. This is done by probing the $\nu_\mu \to \nu_\mu$ oscillation channel through an analysis of tracklike events detected in IceCube DeepCore. The dataset used for this analysis, described in [23], incorporates numerous improvements over previous DeepCore studies in the event selection techniques and the modeling of systematic uncertainties, culminating in a greater statistical power and robustness than earlier results [11].

II. ATMOSPHERIC MUON NEUTRINO SAMPLE

This study uses a dataset representing 7.5 years of livetime from the IceCube DeepCore detector. IceCube consists of 5160 downward-facing digital optical modules (DOMs) that are deployed at depths between 1450–2450 m and distributed over 86 vertical cables [24]. The main array consists of 78 vertical cables that are arranged on a hexagonal lattice with a horizontal spacing of ∼125 m between cables and a vertical spacing of 17 m between DOMs. The remaining eight cables are located in the center of IceCube's footprint with a tighter horizontal separation, between 40 m and 70 m. They contain DOMs with

approximately 35% higher quantum efficiency compared to the main array and are vertically spaced 7 m apart. This central region of the detector forms the DeepCore subarray with a fiducial volume of approximately 10 Mt water equivalent. DeepCore is optimized for the observation of atmospheric neutrinos at energies > 5 GeV and uses the surrounding main array as a veto against muons originating from atmospheric showers that are the most significant background of this analysis [25]. The data acquisition of DeepCore is triggered when a sufficient number of adjacent DOMs within the DeepCore volume record coincident signals that are within a 2.5 μs time window as described in [26].

The triggered events are passed through a series of cuts that reduce the background from random coincidences arising from detector noise and atmospheric muons while keeping most of the atmospheric neutrinos. This analysis uses the same event selection as a previous three-flavor atmospheric ν_μ disappearance analysis described in [23].

A first online filter at the South Pole vetoes events that are consistent with muons entering DeepCore from outside the detector based on hits recorded in the main IceCube array. Additional cuts of increasing complexity applied offline reduce the amount of background by approximately three orders of magnitude [23].

At this stage, the rate is approximately ∼3 μHz and the energy, zenith angle and flavor of each event is reconstructed. The zenith angle reconstruction is a simple geometric χ^2-fit of the observed data to the expectation of Cherenkov light in the absence of light scattering as described in [27]. The cosine of the zenith angle is used as a proxy for the distance traveled by a neutrino between its production in the atmosphere and its interaction in the detector, L. The energy reconstruction is based on a maximum likelihood reconstruction, where the expected charge for each DOM is taken from precomputed tables [28]. Both energy and zenith reconstructions are performed on each event once under a tracklike event hypothesis, indicative of ν_μ and $\bar{\nu}_\mu$ charged current (CC) interactions, and once under a cascadelike hypothesis, characteristic of ν_e CC, most ν_τ CC and all neutral current (NC) interactions. For $\bar{\nu}_\mu$ CC interactions, which are the focus of this analysis, the energy reconstruction at a benchmark value of 20 GeV yields a bias of 0^{+5}_{-4} GeV. The zenith reconstruction at the same energy results in a bias of 6^{+12}_{-6} degrees. In both cases the bias is calculated as the mean of $X_{\text{reco}} - X_{\text{true}}$ and the range contains 50% of the events around this mean. More details of the reconstruction performance for this sample can be found in [23].

The reduced χ^2 from both track and cascade fits, together with the reconstructed track length and information about the location of the event in the detector, are passed into a boosted decision tree (BDT) to calculate a particle identification (PID) score indicating how tracklike, i.e. ν_μ CC-like, an event signature appears. In this analysis, we refer to events with PID values between 0.75 and 1.0 as the "tracks" channel, which consists of ∼93% $\nu_\mu + \bar{\nu}_\mu$ CC events. Backgrounds in this channel consist mostly of atmospheric muons and ν_τ CC events where the τ-lepton decays to a muon with a branching ratio of ∼17%. Events with a PID between 0.55 and 0.75 are referred to as the "mixed" channel, which still mostly consists of $\nu_\mu + \bar{\nu}_\mu$ CC events. Despite a lower purity of ∼65%, this channel still enhances the sensitivity to sterile mixing due to the large number of $\nu_\mu + \bar{\nu}_\mu$ CC events, and is therefore used in the analysis. Since we do not consider cascadelike events with PID < 0.55 in this analysis, the number of electron neutrino interactions in the sample is reduced to below 10%. This reduces the influence of the ν_e oscillation channels, such that $|U_{e4}|^2 = 0$ can be assumed without affecting the analysis. Finally, the events are binned in the reconstructed energy (E_{reco}), the cosine of the reconstructed zenith angle ($\cos(\theta_z) \propto L$) and split by PID channel. We use the same binning as the three-flavor analysis in [23]. In this way, each bin is essentially an independent measurement in L/E that can be used to probe atmospheric neutrino oscillations.

With these criteria we select 21,914 well-reconstructed events for the analysis. The sample contains events spanning a reconstructed energy range from 5 GeV to 150 GeV, with a high purity of ν_μ CC events and a small fraction of atmospheric muons. The total number of events observed in data and expected from MC in each PID channel is provided in Table I. The rates expected from MC simulation are calculated at the best fit point of the analysis.

III. ANALYSIS METHODOLOGY

This analysis employs a *Monte-Carlo forward-folding* method to derive the expectation value of the event counts in the analysis histogram. A large set of MC simulated neutrino events corresponding to approximately 70 yrs of detector livetime has been generated and processed through the chain of filters previously described. These events are weighted according to the expected flux [29] multiplied by the oscillation probability and placed into a histogram with the same binning as the data.

The weighting for each event can be adjusted using the neutrino oscillation parameters as well as a number of nuisance parameters corresponding to the systematic uncertainties in the atmospheric neutrino flux, the neutrino cross sections, the amount of atmospheric muon background and uncertainties of the detector properties. The parameter values are optimized with respect to a modified χ^2 test statistic,

$$\chi^2_{\text{mod}} = \sum_{i \in \text{bins}} \frac{(N_i^{\text{exp}} - N_i^{\text{obs}})^2}{N_i^{\text{exp}} + (\sigma_i^{\text{sim}})^2} + \sum_{j \in \text{syst}} \frac{(s_j - \hat{s}_j)^2}{\sigma_{s_j}^2}, \quad (2)$$

that takes priors on the systematic uncertainties into account as well as the statistical uncertainty in the MC

TABLE I. Observed and expected event rates for different types of particle interactions estimated at the best fit point of the analysis for the individual PID bins and in total.

	All PID			Mixed PID			Track PID		
Event Type	Events	Rate ($1/10^6$ s)	Fraction (%)	Events	Rate ($1/10^6$ s)	Fraction (%)	Events	Rate ($1/10^6$ s)	Fraction (%)
$\nu_\mu + \bar{\nu}_\mu$ CC	17393	73.5	79	6989	29.6	65	10404	44.0	93
$\nu_e + \bar{\nu}_e$ CC	1902	8.0	8.6	1605	6.8	15	298	1.3	2.7
$\nu_\tau + \bar{\nu}_\tau$ CC	599	2.5	2.7	439	1.9	4.1	160	0.7	1.4
$\nu_{\text{all}} + \bar{\nu}_{\text{all}}$ NC	1128	4.8	5.1	936	4.0	8.7	192	0.8	1.7
Atmospheric Muons	971	4.1	4.4	791	3.3	7.3	180	0.8	1.6
All MC	21993	93.0		10760	45.5		11234	47.5	
Data	21914	93.1		10715	45.5		11199	47.6	

prediction, σ_i^{sim}. The index i runs over every bin in the analysis histogram while j runs over all nuisance parameters for which a Gaussian prior has been defined. The expected and observed counts in bin i are N_i^{exp} and N_i^{obs}. The variables s_j, $\hat{s}_j$ and $\sigma_{s_j}^2$ respectively denote the value of the systematic parameter j, its mean and its standard deviation. The total flux normalization is left unconstrained in this analysis, meaning that only effects on the shape of the signal are being considered.

A. Calculation of oscillation probabilities

We calculate neutrino oscillation probabilities using the NUSQUIDS [30,31] package. This package computes state transition probabilities in the interaction picture, where the Hamiltonian is split into the time-independent vacuum oscillation part, H_0, and the variable interaction part, $H_1(t)$, such that

$$H(t) = H_0 + H_1(t). \tag{3}$$

In this picture, the probability to transition to state i after the passage of time t, $p_i(t)$, can be projected out of the state density matrix, $\bar{\rho}(t)$, with

$$p_i(t) = \text{Tr}(\bar{\Pi}^{(\alpha)}(t)\bar{\rho}(t)) \tag{4}$$

where $\bar{\Pi}^{(\alpha)}(t)$ is the projection operator for the flavor state α. The state density at the time of detection is calculated by numerically integrating

$$\partial_t \bar{\rho}(t) = -i[\bar{H}_1(t), \bar{\rho}(t)]. \tag{5}$$

In both equations, the overbar denotes the operator evolution

$$\bar{O}(t) = e^{iH_0 t} O e^{-iH_0 t}. \tag{6}$$

In the mass basis, the vacuum and interaction parts of the Hamiltonian in the $3+1$ model can be written as

$$H_0 = \frac{1}{2E}\text{diag}(0, \Delta m_{21}^2, \Delta m_{31}^2, \Delta m_{41}^2) \tag{7}$$

and

$$H_1(t) = \frac{1}{\sqrt{2}} U_{3+1}^{\text{PMNS},\dagger} \text{diag}(2V_{\text{CC}}(t), 0, 0, V_{\text{NC}}(t)) U_{3+1}^{\text{PMNS}}, \tag{8}$$

respectively. The appearance of a nonzero neutral-current potential V_{NC} in the interaction part of the Hamiltonian is a consequence of the fact that the sterile flavor state does not feel any potential. Therefore, the neutral-current interaction Hamiltonian is no longer diagonal and leads to nontrivial modifications of the neutrino propagation through matter. This method of calculating neutrino oscillation probabilities allows us to apply low-pass filters to the right hand side of Eq. (5) as well as the projection operator in Eq. (4) to greatly improve the efficiency of the calculation. In both cases, the filter replaces $\sin(\omega t)$ and $\cos(\omega t)$ terms that appear in the evaluation of the operator evolution Eq. (6) by zero if the frequency $\omega = \Delta m_{i1}^2/(2E)$ lies above a given threshold.

Oscillation lengths in the presence of an eV-scale mass splitting can be on the order of a few kilometers in the energy range relevant to this analysis. Therefore, we must take care of the assumed neutrino production height in the atmosphere. This is done by averaging the oscillation probability over a range of production heights by replacing the sine and cosine terms in Eq. (4) by their integral over the distance traveled by the neutrino. As a baseline we consider production heights between 10 km and 30 km of altitude. To minimize the effect of this approximation on the analysis, we do not consider events coming from more than $\approx 6°$ above the horizon. As a cross-check, we also varied the range of production height averaging to be between 1 and 20 km and found a negligible impact on the analysis.

In our chosen parametrization,

$$\begin{aligned} U_{3+1}^{\text{PMNS}} = {} & R_{34}(\theta_{34})\tilde{R}_{24}(\theta_{24}, \delta_{24})\tilde{R}_{14}(\theta_{14}, \delta_{14})R_{23}(\theta_{23}) \\ & \times \tilde{R}_{13}(\theta_{13}, \delta_{13})R_{12}(\theta_{12}), \end{aligned} \tag{9}$$

where R_{ij} ($\tilde{R}_{ij}$) represents a (complex) rotation in the ij-plane. The contribution from ν_e events is small enough that $|U_{e4}|^2$ can be neglected without impacting the constraints on the parameters of interest. Therefore, the parametrization of the mixing matrix simplifies to

$$|U_{\mu 4}|^2 = \sin^2(\theta_{24}) \tag{10}$$

$$|U_{\tau 4}|^2 = \sin^2(\theta_{34})\cos^2(\theta_{24}). \tag{11}$$

In contrast to an earlier DeepCore measurement [28], we marginalize over the sterile CP-violating phase δ_{24}, and therefore test a more complete model, similar to [32]. Figure 1 shows the fractional change in the bin counts that would be produced in each bin of the track channel for different combinations of sterile oscillation parameters, where the null-hypothesis is the standard three-flavor oscillation scenario assuming NuFit 4.0 [33] global best fit parameters. In the energy range relevant for this analysis, between 5 and 150 GeV, the observable effect of $|U_{\mu 4}|^2$ is an overall disappearance of muon neutrinos except for the region of maximum disappearance between 15 GeV and 35 GeV as shown in the top row of Fig. 1.

The sensitivity of this analysis to $|U_{\tau 4}|^2$ comes from the matter effects on neutrinos crossing the dense core of the Earth, where a nonzero value of $|U_{\tau 4}|^2$ leads to less disappearance of muon neutrinos between 15 GeV and

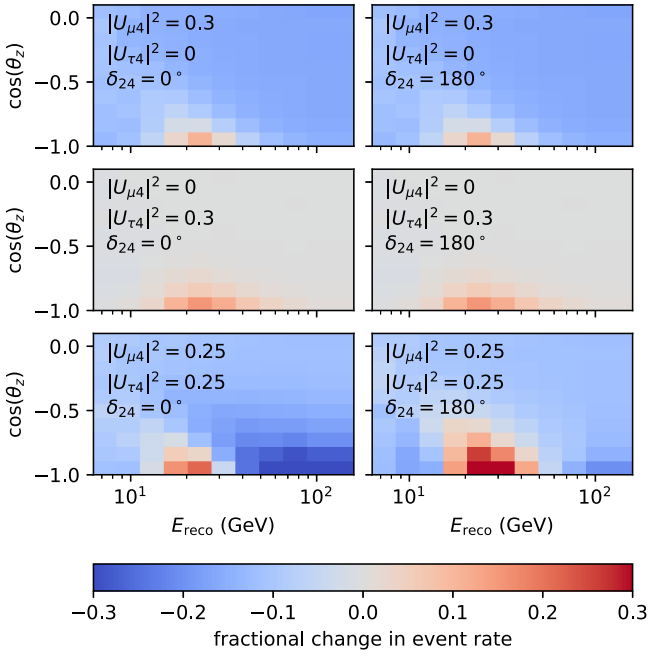

FIG. 1. Sterile oscillation signal in the track channel of the analysis histogram for different combinations of $|U_{\mu 4}|^2$, $|U_{\tau 4}|^2$, and δ_{24}. The fractional change is $(N_{H_1} - N_{H_0})/N_{H_0}$, where N_{H_1} is the bin count for the sterile hypothesis and N_{H_0} the bin count of the null hypothesis without sterile neutrinos.

50 GeV as can be seen in the middle row in Fig. 1. The ability to exploit this matter effect is a unique feature of atmospheric oscillation experiments and is what allows this measurement to be highly sensitive to $|U_{\tau 4}|^2$ when compared to other types of neutrino oscillation experiments. The signal strength is greatest when both matrix elements $|U_{\mu 4}|$ and $|U_{\tau 4}|$ are nonzero, as correlations between them give rise to a signal that is more significant than a simple sum of the individual signals as can be seen in the bottom row of Fig. 1.

The energy resolution of the detector is not sufficient to resolve the rapid oscillation pattern that is produced by the heavy mass eigenstate at the assumed mass-splitting of 1 eV^2. The signal shown in Fig. 1 is the result of these oscillation patterns being effectively averaged out in each bin. As a result of this averaging, the analysis is not sensitive to the precise value of the mass splitting between the sterile and active states and the constraints acquired from this measurement are valid for any mass splitting value ≥ 1 eV^2 up to approximately 100 eV^2, at which point the heavy and active states begin to decohere [34]. This also simplifies the fit procedure because we can keep Δm^2_{41} fixed to 1 eV^2.

B. Systematic uncertainties

The treatment of systematic uncertainties in this analysis follows a similar approach as [23]. Here we provide an overview, highlighting the differences specific to this analysis. A summary of all systematic uncertainties and prior constraints, where applicable, is provided in Table II.

The baseline neutrino flux model [29] is adjusted to account for uncertainties in the primary cosmic ray spectral index [35,37], as well as pion and kaon production uncertainties in air showers outlined in [35] using the MCEq [38] package. Of the subdivisions of the pion and kaon kinematic phase space described in [35], we include two parameters to account for pion uncertainties: $\Delta\pi^{\pm}$ [A-F] which modifies mostly low energy (< 10 GeV) neutrino fluxes; and $\Delta\pi^{\pm}$ [I] to account for higher energy pion production uncertainties. A single parameter, $\Delta\,\mathrm{K}^{+}$ [Y], is used to account for kaon production uncertainties. Variations in other parts of the kaon and pion phase space were found to be insignificant for this analysis.

Cross-section uncertainties for quasi-elastic and resonant neutrino scattering are parametrized based on variations of the respective axial masses in GENIE [39]. To account for uncertainties in the modeling of deep inelastic scattering we follow the same method described in [23], and include a parameter that interpolates between GENIE and CSMS [40] cross-sections. We also include an uncertainty of 20% on the normalization of NC events to account for uncertainties in hadronization processes at the interaction vertex.

Similar to [23], we estimate the baseline muon flux using the cosmic ray composition and flux from [41] and the

TABLE II. Best fit point of all free parameters of the analysis. The significance of the deviation from the nominal point (pull) is given for those parameters for which a Gaussian prior was defined. Parameters with Gaussian priors are allowed to vary within their 3σ range. If a uniform prior was applied to a parameter, its range is given in brackets instead. Blocks of phase space for pion and kaon yields denoted in brackets follow the definitions in [35]. Hole ice parameters p_0 and p_1 are defined in [36].

Parameter	Best fit point	Prior	Pull (σ)
Detector			
DOM efficiency	108%	$(100 \pm 10)\%$	0.812
Hole ice, p_1	0.0408	$[-0.15, 0.1]$	
Hole ice, p_0	−0.589	$[-1.1, 0.5]$	
Ice absorption	98.8%	$(100 \pm 5)\%$	−0.243
Ice scattering	89.5%	$(105 \pm 10)\%$	−1.546
Flux	Changes with respect to Honda *et al.*		
$\Delta\gamma_\nu$	0.091	0.0 ± 0.1	0.910
$\Delta\pi^\pm$ yields [A-F]	+10.6%	$0 \pm 63\%$	0.169
$\Delta\pi^\pm$ yields [I]	+44.6%	$0 \pm 61\%$	0.731
ΔK^+ yields [Y]	−4.01%	$0 \pm 30\%$	−0.134
Cross-section			
M_A^{CCQE}	−0.75%	$0.99\ \text{GeV}^{+25\%}_{-15\%}$	−0.050
M_A^{CCRES}	+1.9%	$1.12\ \text{GeV} \pm 20\%$	0.095
σ_{NC}/σ_{CC}	+0.005	1.0 ± 0.2	0.024
DIS CSMS	0.301	0.0 ± 1.0	0.301
Oscillation			
δ_{24}	180°	[0°, 180°]	
$\sin^2(\theta_{23})$	0.502	[0.12, 0.88]	
$\Delta m^2_{32}/\text{eV}^2$	2.48×10^{-3}	$[2, 3] \times 10^{-3}$	
$\lvert U_{\mu 4}\rvert^2$	0.0045	[0.0, 0.72]	
$\lvert U_{\tau 4}\rvert^2$	0.0031	[0.0, 0.72]	
Atmospheric muons			
Atmospheric μ scale	1.9	[0.0, 3.0]	
Normalization			
A_{eff} scale	0.74	[0.2, 2.0]	

Sibyll2.1 interaction model [42]. Given the minor contribution of atmospheric muons to the dataset used in this analysis, their uncertainty is accounted for by a simple scaling of the muon flux normalization which is left unconstrained in the fit.

The largest contribution to the systematic error budget of this analysis comes from the uncertainties on the detector properties. Just as in [23], the systematic uncertainties related to detector calibration are parametrized by the optical efficiency of the DOMs, the average scattering and absorption coefficients of the natural glacial ice, and two parameters modeling the effects of the column of refrozen ice surrounding the strings [36]. Prior constraints on these parameters, where applicable, are informed by calibration studies as described in [23].

Previously, these effects were quantified on the final histogram using linear regression through predictions from MC sets with varied detector parameters. The downside of this method is that the resulting linear functions are only valid at the flux and oscillation parameters that were chosen to calculate the histograms. For this analysis, we developed an entirely new approach to model detector effects. The new method uses the discrete MC sets to fit a classifier, which estimates the posterior probability that any given event belongs to a particular MC set, given true and reconstructed energy and zenith angles as well as the PID. These posterior probabilities can be used to re-weight each MC event according to its likelihood under a different realization of the detector properties. Because the relationship between true and reconstructed quantities is independent from the initial flux that produced the events, the resulting weight can therefore be applied under any flux and oscillation scenario without modification. The details of this new method are described in [27].

In total there are 18 nuisance parameters in the fit. Additional parameters, for example those related to the atmospheric neutrino flux and ice model uncertainties, were found to have a negligible impact on the analysis. The final set of nuisance parameters that impact this analysis is similar, though not identical, to the analysis presented in [23]. Although the two analyses use the same data sample and binning, there are several difference between them, such as the signal and the modeling of detector calibration uncertainties, which have resulted in slight differences between the nuisance parameters incorporated. However, importantly, the systematic uncertainties with the largest impact remain the same between both analyses. These are the detector calibration uncertainties, $\Delta\gamma_\nu$, and the atmospheric muon scale.

IV. RESULTS

The result of the measurement is compatible with the absence of sterile neutrino mixing and the marginalized constraints for the matrix elements at the 90% and 99% confidence levels are

$$\begin{aligned} |U_{\mu 4}|^2 &< 0.0534(90\%\ \text{CL}), 0.0752(99\%\ \text{CL}), \\ |U_{\tau 4}|^2 &< 0.0574(90\%\ \text{CL}), 0.0818(99\%\ \text{CL}). \end{aligned} \tag{12}$$

In Fig. 2, we show the significance of the deviation between the observed data and the MC prediction at the best fit point of the analysis. Overall we observe good agreement between data and MC, with a p-value of 22.5%. This is also demonstrated by Fig. 3, which shows the data from each bin projected in L/E. For reference we show two additional models with $|U_{\mu 4}|^2$ and $|U_{\tau 4}|^2$ individually set to values at approximately 99% CL. The strong degeneracy between these two parameters when one is fixed to zero is demonstrated by the large overlap between the models. As discussed in Sec. III A, the fast oscillations from a 1 eV^2 scale additional mass splitting are averaged out in this L/E regime, and the signal is instead an overall distortion of the

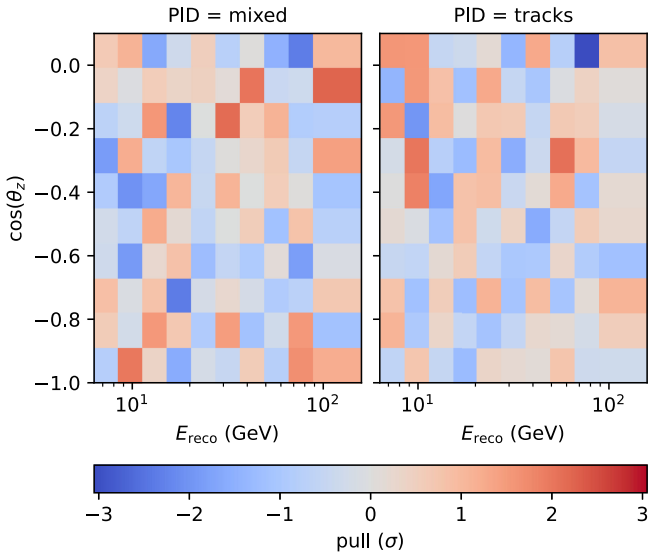

FIG. 2. Bin-wise significance of the deviations between the observed data and the MC prediction at the best fit point of the analysis. The values shown include the Poisson error of the data as well as the error due to finite MC statistics.

spectrum, particularly for long baselines as previously shown in Fig. 1.

The best fit points of all nuisance parameters, shown in Table II, are within prior expectations. The values of the atmospheric neutrino oscillation parameters θ_{23} and Δm^2_{32}, which are treated as free nuisance parameters in this analysis, fit within the 1σ range of the result in [23], although our model fits slightly closer to maximal three-flavor mixing. This is likely due to the slight under-fluctuation of data observed in Fig. 3 for $10^2 \leq L/E \leq 10^3$. The atmospheric muon scale fits to a value of 1.9, almost doubling the rate. This is likely due to a combination of statistical fluctuations, given the small number of muons in the sample, and an underestimation of the baseline atmospheric muon flux, which has been observed in other measurements [43,44]. Our best fit neutrino normalization is also lower than in [23], which can be explained by changes in several correlated parameters, which are shown in Fig. 4. In particular, the neutrino normalization is negatively correlated with the atmospheric muon flux and with the spectral index of the neutrino flux and positively correlated with the scattering coefficient of the ice. In each of these parameters, our fit results have changed with respect to [23] in a way that compensates for the lower normalization.

Since δ_{24} is treated as a free parameter in the fit, these results are valid for both the normal and inverted neutrino mass orderings due to the approximate degeneracy between the mass ordering and the sign of $\cos(\delta_{24})$ as described in [32]. Compared to the previous DeepCore analysis, the limits at 90% CL are improved by a factor of 2.1 and 2.6 for $|U_{\mu 4}|^2$ and $|U_{\tau 4}|^2$, respectively. The limit on $|U_{\tau 4}|^2$ in particular is competitive with limits obtained from global unitarity constraints of the PMNS matrix [21]. The improved sensitivity is largely due to the increase in

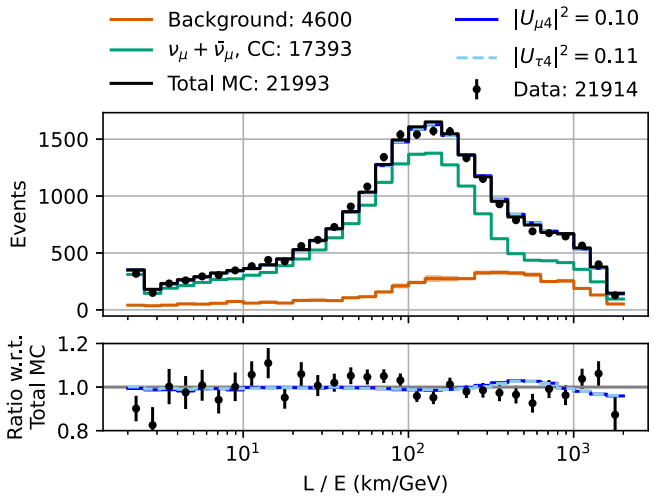

FIG. 3. Post-fit distribution of L/E, compared to the observed data. The background is the sum of atmospheric muon events and all neutrino events except for charged-current ν_μ interactions. The legend shows the number of events in each histogram. Errors include Poisson errors from data as well as the uncertainties due to MC statistics. The outermost bins include overflow events. Alternative hypotheses for $|U_{\mu 4}|^2$ and $|U_{\tau 4}|^2$ are shown in blue after marginalizing over all nuisance parameters.

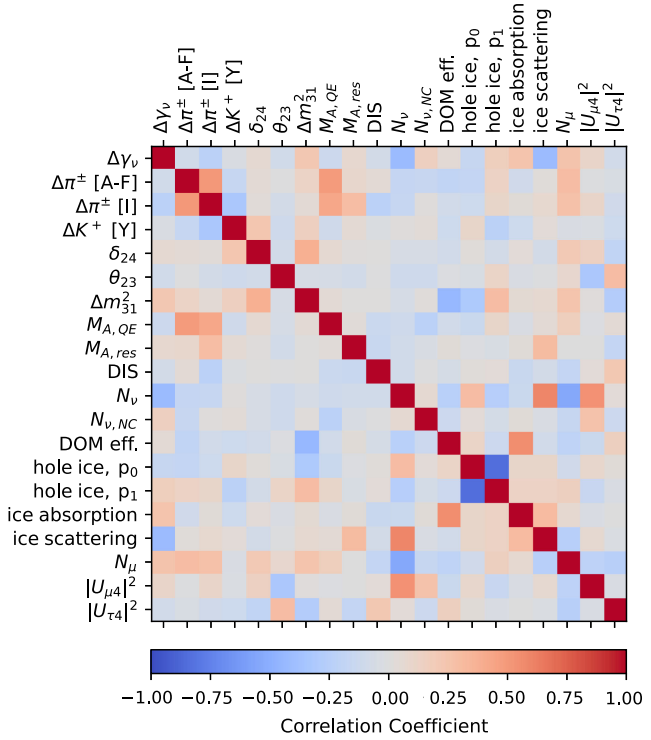

FIG. 4. Pearson correlation coefficients between all free parameters of the analysis, calculated at the best fit point of the analysis.

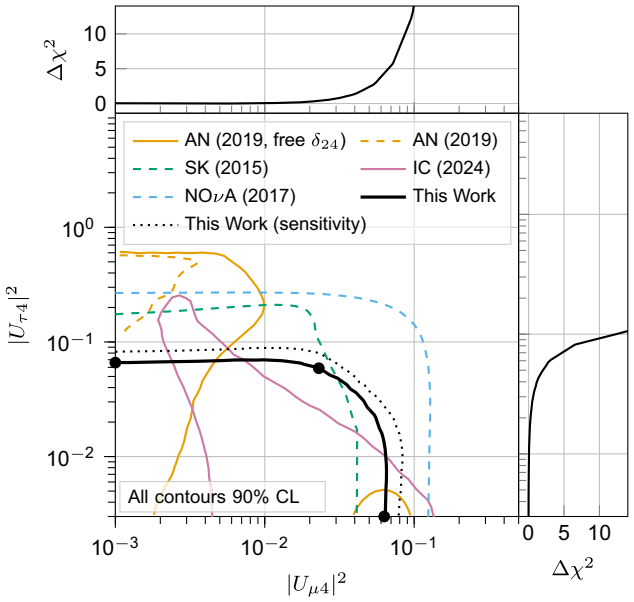

FIG. 5. Contour of the 90% CL limit of this analysis compared to measurements from the ANTARES [32], Super-Kamiokande [45] and NOνA [14] experiments and a recent high-energy IceCube oscillation study [46]. Black dots along the contour of this work indicate where coverage spot-checks were run. The dotted line shows the expected sensitivity of this analysis. Results shown as dashed lines assume $\delta_{24} = 0$.

statistics with a larger data sample, with additional improvements derived from improved detector calibration and treatment of systematic uncertainties.

We performed a scan over $|U_{\mu 4}|^2$ and $|U_{\tau 4}|^2$ with respect to the $\Delta\chi^2 = \chi^2_{\text{mod,best fit}} - \chi^2_{\text{mod,scan point}}$ test statistic and estimated the 90% CL contours using Wilks' theorem assuming two degrees of freedom. The results are shown in Fig. 5. We ran spot-checks of the coverage of the test statistic distribution using 200 pseudodata trials of randomly fluctuated histograms on three points along the contour as shown in Fig. 5. We found that the 90% quantile of the empirical test statistic distribution was lower than the value given by Wilks' theorem on all test points. Thus, the contours drawn in Fig. 5 are a conservative estimate of the correct limits. The limits obtained from the observed data are more stringent than the expected sensitivity, which is also shown in Fig. 5. This is due to the underfluctuation of observed events in the oscillation region that was also reported in [23] and deemed to be compatible with statistical fluctuations therein. Since any nonzero sterile mixing amplitude leads to an increase in the bin counts in the energy range of maximal muon neutrino disappearance as shown in Fig. 1, a statistical under-fluctuation in these bins causes a stronger preference for the null hypothesis and therefore explains the more stringent limits observed in this work.

Compared to other recent $3 + 1$ sterile neutrino searches by IceCube [46,47], which leverage the MSW resonance effect at TeV energies, our methodology investigates sterile neutrino mixing in the 5–150 GeV energy range, which is far from this resonance condition. In addition to the physical effect being probed, systematic uncertainties, especially in neutrino cross sections, vary markedly with energy. The allowed region of phase space from the most directly comparable high-energy IceCube search is shown in Fig. 5. Pursuing both analysis methodologies exploits the full energy range that is observable with the IceCube DeepCore detector, and provides complementary approaches to investigate the $3 + 1$ sterile neutrino landscape.

In summary, the measurement described in this paper adds a new nonobservation to the global picture of $3 + 1$ fits with new competitive limits on $|U_{\mu 4}|^2$ and $|U_{\tau 4}|^2$. This result adds critical information to the ongoing discourse in neutrino physics by addressing the tension between experimental anomalies suggesting active-sterile neutrino mixing and the strong exclusions from other measurements. The sensitivity of this study to $|U_{\tau 4}|^2$, leveraging matter effects in atmospheric neutrino oscillations, exemplifies the importance of diverse experimental approaches in resolving the complex puzzle of neutrino behavior.

ACKNOWLEDGMENTS

The authors gratefully acknowledge the support from the following agencies and institutions: USA—U.S. National Science Foundation-Office of Polar Programs, U.S. National Science Foundation-Physics Division, U.S. National Science Foundation-EPSCoR, U.S. National Science Foundation-Office of Advanced Cyberinfrastructure, Wisconsin Alumni Research Foundation, Center for High Throughput Computing (CHTC) at the University of Wisconsin–Madison, Open Science Grid (OSG), Partnership to Advance Throughput Computing (PATh), Advanced Cyberinfrastructure Coordination Ecosystem: Services & Support (ACCESS), Frontera computing project at the Texas Advanced Computing Center, U.S. Department of Energy-National Energy Research Scientific Computing Center, Particle astrophysics research computing center at the University of Maryland, Institute for Cyber-Enabled Research at Michigan State University, Astroparticle physics computational facility at Marquette University, NVIDIA Corporation, and Google Cloud Platform; Belgium—Funds for Scientific Research (FRS-FNRS and FWO), FWO Odysseus and Big Science programmes, and Belgian Federal Science Policy Office (Belspo); Germany—Bundesministerium für Bildung und Forschung (BMBF), Deutsche Forschungsgemeinschaft (DFG), Helmholtz Alliance for Astroparticle Physics (HAP), Initiative and Networking Fund of the Helmholtz Association, Deutsches Elektronen Synchrotron (DESY), and High Performance Computing cluster of the RWTH Aachen; Sweden—Swedish Research Council, Swedish Polar Research

Secretariat, Swedish National Infrastructure for Computing (SNIC), and Knut and Alice Wallenberg Foundation; European Union—EGI Advanced Computing for research; Australia—Australian Research Council; Canada—Natural Sciences and Engineering Research Council of Canada, Calcul Québec, Compute Ontario, Canada Foundation for Innovation, WestGrid, and Digital Research Alliance of Canada; Denmark—Villum Fonden, Carlsberg Foundation, and European Commission; New Zealand—Marsden Fund; Japan—Japan Society for Promotion of Science (JSPS) and Institute for Global Prominent Research (IGPR) of Chiba University; Korea—National Research Foundation of Korea (NRF); Switzerland—Swiss National Science Foundation (SNSF).

[1] A. Aguilar-Arévalo *et al.* (LSND Collaboration), Evidence for neutrino oscillations from the observation of $\bar{\nu}_e$ appearance in a $\bar{\nu}_\mu$ beam, Phys. Rev. D **64**, 112007 (2001).
[2] A. A. Aguilar-Arévalo *et al.* (MiniBooNE Collaboration), Updated MiniBooNE neutrino oscillation results with increased data and new background studies, Phys. Rev. D **103**, 052002 (2021).
[3] W. Hampel *et al.*, Final results of the 51Cr neutrino source experiments in GALLEX, Phys. Lett. B **420**, 114 (1998).
[4] V. Barinov *et al.*, Results from the Baksan Experiment on Sterile Transitions (BEST), Phys. Rev. Lett. **128**, 232501 (2022).
[5] J. N. Abdurashitov *et al.*, Measurement of the response of a Ga solar neutrino experiment to neutrinos from a ^{37}Ar source, Phys. Rev. C **73**, 045805 (2006).
[6] Z. Maki, M. Nakagawa, and S. Sakata, Remarks on the unified model of elementary particles, Prog. Theor. Phys. **28**, 870 (1962).
[7] M. Dentler, Á. Hernández-Cabezudo, J. Kopp, P. Machado, M. Maltoni, I. Martínez-Soler, and T. Schwetz, Updated global analysis of neutrino oscillations in the presence of eV-scale sterile neutrinos, J. High Energy Phys. 08 (2018) 010.
[8] A. Diaz, C. Argüelles, G. Collin, J. Conrad, and M. Shaevitz, Where are we with light sterile neutrinos?, Phys. Rep. **884**, 1 (2020).
[9] M. G. Aartsen *et al.* (IceCube Collaboration), eV-scale sterile neutrino search using eight years of atmospheric muon neutrino data from the icecube neutrino observatory, Phys. Rev. Lett. **125**, 141801 (2020).
[10] M. G. Aartsen *et al.* (IceCube Collaboration), Searching for eV-scale sterile neutrinos with eight years of atmospheric neutrinos at the IceCube Neutrino Telescope, Phys. Rev. D **102**, 052009 (2020).
[11] M. G. Aartsen *et al.*, Search for sterile neutrino mixing using three years of IceCube DeepCore data, Phys. Rev. D **95**, 112002 (2017).
[12] P. Abratenko *et al.* (MicroBooNE Collaboration), Search for an excess of electron neutrino interactions in MicroBooNE using multiple final-state topologies, Phys. Rev. Lett. **128**, 241801 (2022).
[13] P. Abratenko *et al.* (MicroBooNE Collaboration), Search for an anomalous excess of charged-current quasielastic ν_e interactions with the MicroBooNE experiment using Deep-Learning-based reconstruction, Phys. Rev. D **105**, 112003 (2022).
[14] S. Edayath, A. Aurisano, A. Sousa, G. Davies, L. Suter, and S. Yang, Sterile neutrino search in the NOvA Far Detector, in Proceedings of the APS Division of Particles and Fields (2017), arXiv:1710.01280.
[15] P. Adamson *et al.* (MINOS+ Collaboration), Search for sterile neutrinos in MINOS and MINOS+ using a two-detector fit, Phys. Rev. Lett. **122**, 091803 (2019).
[16] Z. Atif *et al.* (RENO and NEOS Collaborations), Search for sterile neutrino oscillations using RENO and NEOS data, Phys. Rev. D **105**, L111101 (2022).
[17] H. Almazán *et al.* (STEREO Collaboration), Improved sterile neutrino constraints from the STEREO experiment with 179 days of reactor-on data, Phys. Rev. D **102**, 052002 (2020).
[18] H. Almazán *et al.* (STEREO Collaboration), STEREO neutrino spectrum of ^{235}U fission rejects sterile neutrino hypothesis, Nature (London) **613**, 257 (2023).
[19] I. Alekseev *et al.* (DANSS Collaboration), Search for sterile neutrinos at the DANSS experiment, Phys. Lett. B **787**, 56 (2018).
[20] F. P. An *et al.* (Daya Bay Collaboration), Improved search for a light sterile neutrino with the full configuration of the Daya Bay experiment, Phys. Rev. Lett. **117**, 151802 (2016).
[21] Z. Hu, J. Ling, J. Tang, and T. Wang, Global oscillation data analysis on the 3ν mixing without unitarity, J. High Energy Phys. 01 (2021) 124.
[22] Aghanim N. *et al.* (Planck Collaboration), Planck 2018 results-VI. Cosmological parameters, Astron. Astrophys. **641**, A6 (2020).
[23] R. Abbasi *et al.* (IceCube Collaboration), Measurement of atmospheric neutrino mixing with improved IceCube DeepCore calibration and data processing, Phys. Rev. D **108**, 012014 (2023).
[24] M. G. Aartsen *et al.*, The IceCube neutrino observatory: Instrumentation and online systems, J. Instrum. **12**, P03012 (2017).
[25] R. Abbasi *et al.* (IceCube Collaboration), The design and performance of IceCube DeepCore, Astropart. Phys. **35**, 615 (2012).
[26] J. L. Kelley (IceCube Collaboration), Event triggering in the IceCube data acquisition system, AIP Conf. Proc. **1630**, 154 (2014).
[27] L. Fischer, R. Naab, and A. Trettin, Treating detector systematics via a likelihood free inference method, J. Instrum. **18**, P10019 (2023).

[28] A. Terliuk, Measurement of atmospheric neutrino oscillations and search for sterile neutrino mixing with IceCube DeepCore, Ph.D. thesis, Humboldt-Universität zu Berlin, Mathematisch-Naturwissenschaftliche Fakultät, 2018, 10.18452/19304.

[29] M. Honda, M. Sajjad Athar, T. Kajita, K. Kasahara, and S. Midorikawa, Atmospheric neutrino flux calculation using the NRLMSISE-00 atmospheric model, Phys. Rev. D **92**, 023004 (2015).

[30] C. A. Argüelles Delgado, J. Salvadó, and C. N. Weaver, A simple quantum integro-differential solver (SQuIDS), Comput. Phys. Commun. **196**, 569 (2015).

[31] D. Argüelles *et al.*, nuSQuIDs, https://github.com/arguelles/nuSQuIDS.

[32] A. Albert *et al.* (ANTARES Collaboration), Measuring the atmospheric neutrino oscillation parameters and constraining the 3+1 neutrino model with ten years of ANTARES data, J. High Energy Phys. 06 (2019) 113.

[33] I. Esteban, M. C. González-García, A. Hernández-Cabezudo, M. Maltoni, and T. Schwetz, Global analysis of three-flavour neutrino oscillations: synergies and tensions in the determination of θ_{23}, δ_{CP}, and the mass ordering, J. High Energy Phys. 01 (2019) 106.

[34] B. Jones, Dynamical pion collapse and the coherence of conventional neutrino beams, Phys. Rev. D **91**, 053002 (2015).

[35] G. D. Barr, T. K. Gaisser, S. Robbins, and T. Stanev, Uncertainties in atmospheric neutrino fluxes, Phys. Rev. D **74**, 094009 (2006).

[36] P. Eller *et al.* (IceCube Collaboration), A model independent parametrization of the optical properties of the refrozen IceCube drill holes, Proc. Sci. ICRC2023 (**2023**) 1034 [arXiv:2307.15298].

[37] J. Evans, D. G. Gámez, S. D. Porzio, S. Söldner-Rembold, and S. Wren, Uncertainties in atmospheric muon-neutrino fluxes arising from cosmic-ray primaries, Phys. Rev. D **95**, 023012 (2017).

[38] A. Fedynitch, F. Riehn, R. Engel, T. K. Gaisser, and T. Stanev, Hadronic interaction model sibyll 2.3c and inclusive lepton fluxes, Phys. Rev. D **100**, 103018 (2019).

[39] C. Andreopoulos, C. Barry, S. Dytman, H. Gallagher, T. Golan, R. Hatcher, G. Perdue, and J. Yarba, The GENIE neutrino monte carlo generator: Physics and user manual, arXiv:1510.05494.

[40] A. Cooper-Sarkar, P. Mertsch, and S. Sarkar, The high energy neutrino cross-section in the Standard Model and its uncertainty, J. High Energy Phys. 08 (2011) 042.

[41] T. K. Gaisser, Spectrum of cosmic-ray nucleons, kaon production, and the atmospheric muon charge ratio, Astropart. Phys. **35**, 801 (2012).

[42] E.-J. Ahn, R. Engel, T. K. Gaisser, P. Lipari, and T. Stanev, Cosmic ray interaction event generator SIBYLL 2.1, Phys. Rev. D **80**, 094003 (2009).

[43] F. Riehn, R. Engel, and A. Fedynitch, Sibyll★, Astropart. Phys. **160**, 102964 (2024).

[44] S. Aiello *et al.* (KM3NeT Collaboration), Atmospheric muons measured with the KM3NeT detectors in comparison with updated numeric predictions, Eur. Phys. J. C **84**, 696 (2024).

[45] K. Abe *et al.* (Super-Kamiokande Collaboration), Limits on sterile neutrino mixing using atmospheric neutrinos in Super-Kamiokande, Phys. Rev. D **91**, 052019 (2015).

[46] R. Abbasi *et al.* (IceCube Collaboration), Exploration of mass splitting and muon/tau mixing parameters for an eV-scale sterile neutrino with IceCube, arXiv:2406.00905.

[47] R. Abbasi *et al.* (IceCube Collaboration), A search for an eV-scale sterile neutrino using improved high-energy ν_μ event reconstruction in IceCube, arXiv:2405.08070.